Article

Effects of Grain Size on the Thermoelectric Properties of Cu₂SnS₃: An Experimental and First-Principles Study

Ketan Lohani, Himanshu Nautiyal, Narges Ataollahi, Krishnendu Maji, Emmanuel Guilmeau,* and Paolo Scardi*

Cite This: https://doi.org/10.1021/acsaem.1c02377

Read Online

ACCESS | Metrics & More | Article Recommendations | Supporting Information

ABSTRACT: Cu−Sn-based sulfides are earth-abundant and nontoxic compounds of special interest for low-cost energy harvesting applications. In the present work, we have investigated the effect of grain size on the thermoelectric properties of Cu_2SnS_3 (CTS). Three dense CTS samples with nanometric grains were produced by mechanical alloying combined with spark plasma sintering, preserving the small size of crystalline domains to 12, 25, and 37 nm, respectively. The experimental results show that the Seebeck coefficient (S) and electrical resistivity (ρ) decrease with decreasing domain sizes, while the thermal conductivity (κ) increases. A smaller domain size correlates with a lower resistivity and a degenerate semiconductor-like behavior due to higher carrier concentration. At the same time, our synthesis method leads to materials with very low lattice thermal conductivity, thanks to the nanometric size of grains and structural disorder. As a result, the sample with the smallest grain size exhibits the highest zT of ∼0.4 at 650 K. First-principles density functional theory (DFT) simulations on various CTS crystallite surfaces revealed localized states near the Fermi level and the absence of band gap, indicating the metallic nature of the surfaces. Various CTS systems were tested by DFT, showing the following order of increasing formation energy: stoichiometric CTS, Cu vacancy, Cu-rich, Sn vacancy, and Sn-rich.

KEYWORDS: Cu_2SnS_3, grain size effect, DFT, thermoelectric Cu_2SnS_3, spark plasma sintering, p-type semiconductor
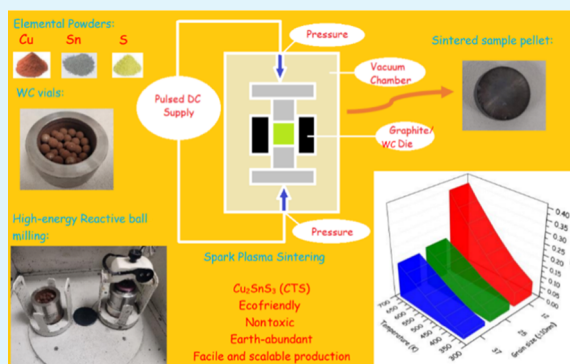
INTRODUCTION

Most commercially available thermoelectric (TE) devices use toxic and scarce materials, making them expensive and potentially hazardous, for example, Sb_2Te_3, Bi_2Te_3, and so forth. In recent years, the search for high-performance, nontoxic, ecofriendly, and earth-abundant TE materials has led to the exploration of multinary sulfides.[1,2] Chalcogenides,[3] colusites,[4,5] and other metal-based sulfides[6,7] could be viable alternatives to existing materials.[8] Cu-based sulfides have low formation energy so that it is possible to produce them by short-period reactive milling using a planetary or vibrating mill. As also shown in the present work, high-energy reactive ball milling, also called mechanical alloying, can be employed with success to synthesize new and disordered phases. In addition, milling offers the advantage of facile and scalable production for industrial use.[9]

The energy conversion efficiency of a TE material is determined by a dimensionless figure of merit (zT) expressed as $zT = S^2/\rho\kappa * T$, where S, ρ, κ, and T are the Seebeck coefficient, electrical resistivity, thermal conductivity, and absolute temperature, respectively. S^2/ρ is referred to as the power factor (PF). The Seebeck coefficient and electrical resistivity are strongly dependent on the carrier concentration (n), mobility (μ), and effective mass of the charge carriers (m^*) (see eqs 1 and 2 below). A low carrier concentration and high effective mass of charge carriers can increase the Seebeck coefficient, but it also penalizes the electrical conductivity (σ) and *vice versa.*[1,10]

$$S = Am^*\left(\frac{\pi}{3n}\right)^{2/3}T \tag{1}$$

$$\sigma = ne\mu \tag{2}$$

$$\kappa_e = \frac{LT}{\rho} \tag{3}$$

where A, e, and L represent a constant, charge of an electron, and the Lorenz number, respectively.

ACS Publications

A

Table 1. Sample Names, Sintering Conditions, Densities, Phase Purity, and Average Grain Size for Various CTS Samples

sample name	sintering die	sintering pressure (MPa)	sintering temperature (°C)	dwell time (min)	density (g/cm³)	weight fraction (±1%)		average domain size (±10 nm)
						disordered-CTS	secondary phase name	
A	WC	500	400	60	4.06	99	SnO_2-1	12
B	graphite	64	512	30	4.52	100		25
C	graphite	64	500	30	4.45	99	SnO_2-1	37

Besides high *PF*, TE materials also require low thermal conductivity (κ), composed of a lattice (κ_l) and an electronic contribution (κ_e), combined as $\kappa = \kappa_l + \kappa_e$. The lattice contribution can be decreased by increasing the grain boundary density, vacancies, defects, impurities, strain, and so forth. Differently, κ_e shows a strong dependence on the electrical resistivity, as in the Wiedemann−Franz law (see eq 3).[5] More recently, the determination of the TE quality factor (β) given by $\beta \propto \mu_0 m_{dos}{*}^{3/2}/\kappa_l$ (where μ_0 and $m_{dos}{*}$ are the nondegenerate mobility and density of state effective mass, respectively) is in practice for the simultaneous optimization of all TE parameters.[11,12]

$Cu_{2+x}Sn_{1-x}S_3$(CTS) polymorphs are studied for many applications such as photovoltaics, transistors, LEDs, and TE materials. A recent study has also suggested a potential use of CTS quantum dots for photodetector applications.[13] CTS polymorphs have been extensively studied as p-type TE materials showing moderately high *PF* with high or low thermal conductivity, depending on whether the crystal structure is ordered or disordered.[14−16] To increase the TE performance, different cationic substitutions have been investigated with the aim to tune the carrier concentration and to introduce structural disorder. Among the various studies, Zhao *et al.* have reported the highest $zT \sim 0.9$ (at $T > 700$ K) so far by simultaneous cobalt and antimony doping.[17]

Zhai *et al.*[18] and Shigemi *et al.*[19] have shown that the hybridization of Cu 3d and S 3p orbitals in the valence band (VB) is responsible for the p-type nature of CTS. Heavy acceptor doping due to unfilled d-orbitals of Co,[20] Cu,[21] Ni,[17] Fe,[22] and Mn[23] enhances the density-of-state (DOS) effective mass of carriers (holes) and electrical conductivity, resulting in a high *PF* ~10 μW/cm K^2 around 700 K. Cationic substitution also transforms the CTS crystal structure from ordered (monoclinic *Cc*)[24] to tetragonal $I\bar{4}2m$[25] and disordered (cubic: $F\bar{4}3m$).[14] In most of the cases, a mixture of different phases is obtained. Deng *et al.*[21] have shown the influence of the Cu/Sn ratio in $Cu_{2+x}Sn_{1-x}S_3$ on the electrical and thermal properties. More recently, Pavan Kumar *et al.*[16] have discovered a new ordered monoclinic structure $Cu_5Sn_2S_7$ by increasing the Cu/Sn ratio up to $x = 0.15$, leading to a specific ordering of Cu and Sn in the structure. In summary, the hole doping in CTS compounds, induced by the substitution of Cu, Sn, or S by aliovalent cations, or by Cu for Sn substitution, increases the carrier concentration. Disordering phenomena, usually induced by the cationic/anionic substitution, scatter the phonon waves more effectively, resulting in a higher TE figure of merit.

The disordered cubic CTS and Cu_2SnSe_3 (CTSe) phases can also be produced and stabilized without chemical alteration.[15,26,27] The optical absorption measurements revealed a lower band gap for the disordered CTS/Se polymorphs. The lower band gap enhances the carrier concentration, resulting in a higher *PF* compared to its ordered polymorph. Furthermore, in a theoretical study,

Baranowski *et al.*[28] have also reported band tailing and midgap states for the disordered CTS phase.[26,28] The structural disorder introduces potential energy fluctuations in the lattice that allow energy levels within the forbidden gap, responsible for the band tailing and reduced band gap. Moreover, Dahule *et al.*[29] have studied the electronic structure properties of (200) and (−131) surfaces of monoclinic CTS and have shown their metallic character. It is worth mentioning that the metallic character was confirmed using different potentials, including the Heyd−Scuseria−Ernzerhof potential, which results in a better estimation of the band gap.

In terms of synthesis, the literature suggests a three-step top-down approach to produce CTS samples for TE applications. First, CTS is produced from the elemental powders (Cu, Sn, S, and dopant elements) using an extended high-temperature solid-state reaction.[14] In the second step, the grain size is sometimes reduced by ball milling. Finally, high-density pellets are produced using spark-plasma sintering (SPS) or hot pressing. This approach results in highly crystalline materials with average domain sizes ranging from half to several microns. This synthesis method requires a long annealing time at high temperatures, which is time- and resource-consuming.

Alternatively, CTS compounds, as many other Cu-based sulfides, can be produced by combined high-energy reactive ball milling (mechanical alloying) and SPS or hot pressing.[16,30] Mechanical alloying allows us to produce fine, homogeneous, precrystallized, and highly reactive powders, which usually lead to high-purity, crystalline, and dense samples after sintering with small grain and crystallite sizes. Furthermore, a highly dense disordered CTS polymorph can be stabilized without any chemical substitution.[9]

The present work aims to shed light on the degenerate semiconductor-like behavior of nanocrystalline CTS samples. Three dense CTS samples were produced using powder synthesized by high-energy reactive ball milling and SPS. We have investigated the effects of grain size on the TE properties. Structural and microstructural analyses suggested a stoichiometry deviation in CTS phases sintered at low temperature, together with a very small crystallite and grain size. *Ab initio* calculations using density functional theory (DFT) indicated the metallic nature of CTS surfaces, leading to a degenerate semiconductor-like trend with temperature. Further evidence is presented on the formation energies for various CTS systems with vacancies and chemical deviations.

■ MATERIALS AND METHODS

Experimental Section. Elemental powders (Cu, Sn, and S) were weighted in a stoichiometric ratio and fed in WC vials with WC balls. A Fritsch PULVERISETTE-4 mill was operated for 1 h, producing ~6 g of the as-milled CTS powder. The entire production process was performed in a glovebox with an argon-filled environment. During the milling, no lubricant was introduced to avoid any contamination. The production of CTS powder by high-energy ball milling of elemental powders and binary sulfides is discussed in detail elsewhere.[15,26]

The as-milled powder was sintered using a SPS machine (FCT HPD 25) at various temperatures and pressures to optimize the sintering conditions (Table 1). The relative densities of the samples are 86, 96, and 94% for sample A, B, and C, respectively.

Structural analysis was performed using X-ray diffraction (XRD). XRD data were collected in $\theta/2\theta$ Bragg−Brentano geometry using a PANalytical X'Pert Pro diffractometer equipped with a Cu Kα (λ = 1.5406 Å) source. Micrographs and energy-dispersive X-ray (EDX) spectroscopy analyses were collected using a JEOL JSM 7200F scanning electron microscope equipped with an EDX X-Flash Bruker detector.

The electrical resistivity (ρ) and Seebeck coefficient (S) were measured simultaneously from 300 up to 700 K on bar-shaped samples of typical dimensions $2 \times 3 \times 10$ mm^3 using an ULVAC-ZEM3 instrument under partial helium pressure. A NETZSCH LFA-457 apparatus was used for measuring the thermal diffusivity under argon flow. The thermal conductivity (κ) was determined as the product of the geometrical density, the thermal diffusivity, and the theoretical heat capacity using the Dulong−Petit approximation. The lattice contribution to the thermal conductivity (κ_l) was determined by subtracting the estimated electronic component (κ_e) from the measured total thermal conductivity, κ. The measurement uncertainties are estimated to be 6% for the Seebeck coefficient, 8% for the electrical resistivity, 11% for the thermal conductivity, and 16% for the final dimensionless figure of merit.

Hall effect measurements at RT were carried out using a physical property measurement system (Quantum Design) under an applied magnetic field of 9 T.

COMPUTATIONAL METHODS

The electronic structure calculations were performed using DFT as implemented in the Vienna *ab initio* simulation package.[31,32] The interaction between electrons and ions was described using the projector-augmented-wave (PAW) method. The generalized gradient approximation with Perdew−Burke−Ernzerhof[33] electron exchange−correlation was used for the calculations.

We have performed the calculations for (001), (010), and (100) slabs of monoclinic CTS and two disordered CTS cells with sulfur termination. We considered two cases for the disordered cell, one with the Cu-rich and the other with Sn-rich atomic layer below the terminating sulfur layer. For all the calculations, CTS stoichiometry was preserved. A vacuum of 15 Å was created to minimize the interaction between the periodic copies. In the disordered cells, the atoms of the lower four layers were fixed in a position, whereas the atoms of the upper four layers were free to move. Relaxation was performed with a plane-wave kinetic energy cutoff and an electronic convergence of 350 and 10^{-5} eV, respectively. The involvement of core electrons was seized by freezing. Only 3d^{10}4s^1, 4d^{10} 5s^2 5p^2, and 3s^2 3p^4 electrons were treated as valence electrons for Cu, Sn, and S, respectively. The cell parameters were fixed, whereas the atomic position was allowed to change for relaxation. The electronic convergence was set to 10^{-6} eV for DOS calculations. Brillion zone sampling was performed on a k-point grid of $9 \times 9 \times 1$ and $5 \times 5 \times 1$ for monoclinic slabs and disordered cells, respectively. The k-mesh was reduced for the disordered cell due to its larger size.

The formation energy calculations were performed on Cu-rich, Cu-vacant, Sn-rich, and Sn-vacant cells. For these calculations, the plane wave kinetic energy cutoff and electronic convergence were changed to 400 and 10^{-6} eV, respectively. A Monkhorst−Pack[34] k-point mesh of $7 \times 7 \times 7$ (centered at the gamma point) was used to integrate the Brillion zone. One atom was removed from the supercell, and the remaining atoms were allowed to relax for the vacancy calculations. The off-stoichiometry calculations were performed on a supercell of 72 atoms with a stable monoclinic phase, where one Cu atom was replaced by one Sn atom and *vice versa*, respectively, for the Sn-rich and Cu-rich simulations.

RESULTS AND DISCUSSION

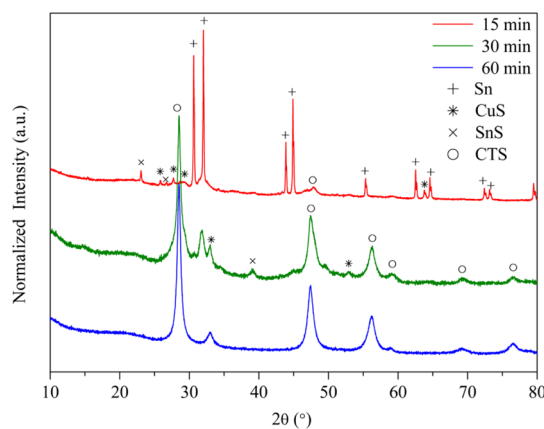XRD patterns collected on the as-milled powder with increasing milling times are shown in Figure 1. Due to its

Figure 1. XRD patterns for the powder milled for 15, 30, and 60 min.

low formation energy, short milling of 15 min led to the formation of binary sulfides, especially CuS. As the milling time was increased to 30 min, the appearance of diffraction peaks of sphalerite-type structures can be noticed. However, unreacted SnS and Sn powder were still present in the sample. With the further increase of the milling time to 1 h, the as-milled powder showed four broad diffraction peaks, implying the formation of a sphalerite-type crystal structure. It is worth mentioning here that, among all the elements, Sn incorporated last in the CTS system. Broad Bragg-peaks with diffuse backgrounds imply that the one-hour milled powder consists of less crystalline CTS grains with a small domain size.

SEM−EDX data collected on 60 min milled powder at full-frame image showed the presence of stoichiometric CTS. On the same sample, various micrographs and EDX data were collected at different magnifications from different parts of the SEM grid. It indicated that the as-milled powder has a nonhomogeneous chemical distribution with a small domain size, which tends to agglomerate in larger particles (Figure S1).

High-density bulk CTS samples were produced by SPS under different sintering conditions (listed in Table 1). Sintered samples maintained the same Bragg-peak positions as the as-milled powder. However, sharper Bragg peaks for sintered samples indicate an increased crystallinity and crystallite size. XRD line profile analysis was performed by the Rietveld method[35] using Topas 7 software.[36] We employed the whole powder pattern modeling macro[37] to simulate the peak profile. The instrumental profile was obtained from a LaB$_6$ standard sample.[38] A nine-point Chebyshev polynomial and a 1/x-function were used to simulate the background and low-angle intensity, respectively. Subsequently, zero shift and other parameters were systematically refined.[39] During the refinement, the variation of the Debye−Waller coefficients (thermal factors) was restricted between 0 and 2 for all atoms. For all the samples discussed below, the goodness of fit was ∼1.1−1.3.

Disordered CTS has a zinc-blende (ZnS)-like (cubic) close-packed face-centered structure, which arranges its atoms in the (216) space group. The 4a Wyckoff position is occupied by Cu and Sn atoms with occupancy 2/3 and 1/3, respectively, while the 4c site is occupied by S atoms with occupancy 1. The

C
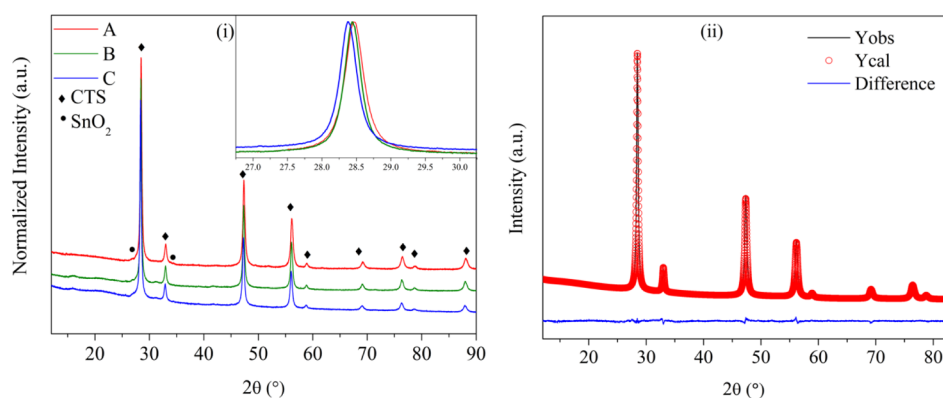
Figure 2. (i) XRD patterns of samples sintered under various conditions.; (ii) Rietveld refinement data for sample A collected (Yobs), calculated (Ycal), difference (difference) pattern. See Figure S2 for the Rietveld refinement data for samples B and C.
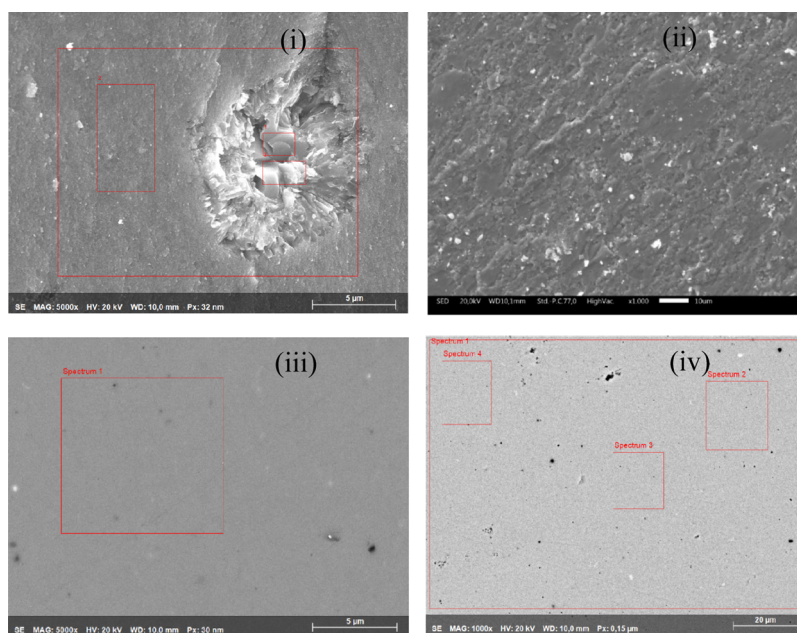
Figure 3. (i) SEM micrograph of the surface of SPS sintered sample A showing a compact sample with almost no pores and the presence of SnS; (ii) WC particles on one of the samples (bright spots in the micrograph, identified by EDX); (iii) micrographs of polished samples A and (iv) B. EDX data are provided in Table S1.

lattice parameter, phase density, and cell volume determined from Rietveld refinement were 5.43 Å, 4.71 g/cm^3, and 160.50 Å^3, respectively. No microstrain was observed for any sample. The average domain size and the weight fraction of CTS and secondary phases are listed in Table 1 for different sintering conditions. All the samples showed disordered cubic CTS structures. However, a small amount (weight fraction <0.5%) of SnO$_2$ was observed for samples A and C. For sample B (see Figure 2a), two Bragg peaks around $2\theta \sim 16$ and $\sim 31°$ were observed. Sample B may have a small amount of the monoclinic phase. However, the two peaks are quite broad which makes it hard to quantify the monoclinic phase reliably, and it is certainly below 1% in weight.

The sizes of crystalline domains were estimated as 12 ± 10, 25 ± 10, and 37 ± 10 nm for samples A, B, and C, respectively. The reported average grain size for high-density CTS samples prepared by the three-step method (discussed in the Introduction) is in the range of 500−600 nm,[25] and in some cases, micron-size grains are also reported.[20] In contrast, traditionally sintered samples (without applying pressure)

showed smaller grains, domain size ranging from ∼50 nm to a few 100 nm, and low density.[15] The mechanical alloying combined with the SPS method proposed here constrained the grain size below 50 nm[30] while promoting densification at a relatively low sintering temperature.

SEM micrographs on bulk samples reveal a dense microstructure, that is, highly intact grains with almost no porosity (shown in Figure 3, S3 and S4). Unlike the as-milled powder, EDX analysis on the sintered samples revealed a homogeneous chemical distribution, with the exception of sample A, in which a small amount of SnS was found, likely due to an incomplete reaction at 400 °C (Figures 3i, S3, and S5). Some bright spots in the micrographs revealed traces of WC particles. However, WC and SnS signals were not observed in the XRD patterns because of their small weight fraction, which was below the detection limit (≪1%). Comparative SEM−EDX analysis was performed on samples A and B (before and after polishing), and SEM−EDX data are shown in the Supporting Information (Figures S3−S6). Sample A has a higher amount of the SnS phase compared to sample B, probably due to a lower sintering

temperature. However, the matrix composition for both samples is similar, suggesting that stoichiometric deviation in CTS grains is quite small. These micrographs also confirm that the average grain size is much smaller than the magnification of the microscope allows to see.

Figures 4(i,ii) shows the absolute Seebeck coefficient (S) and resistivity (ρ), respectively, for the CTS samples in Table
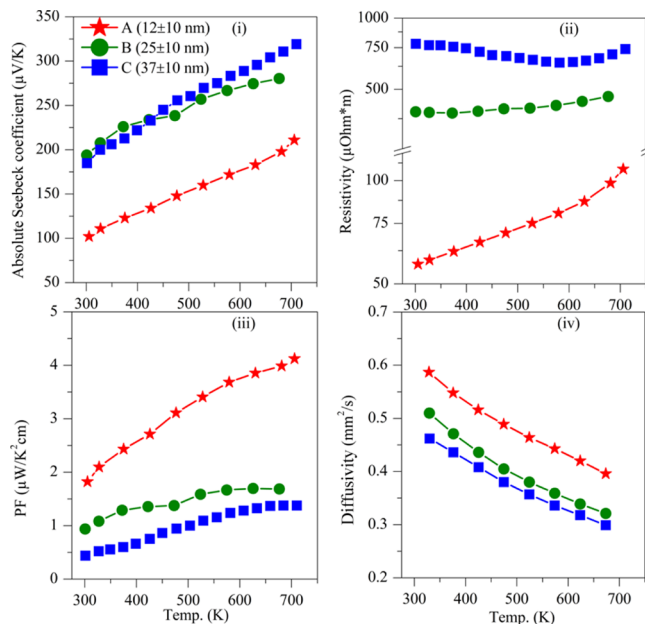

Figure 4. Temperature-dependent (i) absolute Seebeck coefficient, (ii) resistivity, (iii) PF, and (iv) diffusivity for sintered samples A, B, and C.

1. Although there is a variation in the values of S, all the samples show a positive Seebeck coefficient increasing with temperature. Samples A, B, and C present $S \sim 100$, 180, and 160 μV/K, respectively, at room-temperature (RT), which are lower than the reported RT values for the CTS compound ($S \sim 500-700$ μV/K).[16,21,26] A general trend of increasing values of the Seebeck coefficient with increasing sintering temperature and grain size can be observed. The Cu−Sn−S-based

systems exist in numerous phases, such as Cu_2SnS_3,[15] Cu_3SnS_4,[40] $Cu_5Sn_2S_7$,[16] $Cu_7Sn_3S_{10}$[41] and so forth.[2] Mostly, these systems show a p-type semiconducting nature due to the unfilled Cu 3d-orbitals. Additionally, Cu−S bonds in Cu−Sn−S-based systems form a three-dimensional conduction network which enhances their electrical conductivity.[14]

It is well known that undoped CTS is highly resistive with a nondegenerate semiconductor-like trend in temperature owing to its low carrier concentration.[15] However, samples A and B show a degenerate semiconductor-like nature, whereas sample C, with the largest S (~ 320 μV/K, above 650 K), shows a nondegenerate trend up to ~ 650 K. As expected, samples with a higher Seebeck coefficient have higher electrical resistivity and *vice versa*, but a trend of decreasing electrical resistivity can also be observed with the decrease in the crystalline domain size. It is worth mentioning here that off-stoichiometry in CTS compounds can lead to similar results, although such deviations should have a Cu/Sn ratio >2. In fact, Deng *et al.*[21] show that an excess of Cu in $Cu_{2+x}Sn_{1-x}S_3$ ($x \geq 0.016$) changes the electrical resistivity from a nondegenerate to degenerate behavior. This suggests that the CTS phase, especially when sintered at low T (400 °C, sample A), is nonstoichiometric.

In general, a small grain size leads to a higher Seebeck coefficient due to the scattering of charge carriers by the grain boundary, otherwise known as energy filtering.[42] This, however, decreases the mobility and, in turn, increases the electrical resistivity. The lower grain size is also crucial in the suppression of thermal conductivity by scattering phonon waves effectively. The results shown here contrast with the energy filtering mechanism. The samples with smaller domains are more conductive, and we observe a trend of increasing resistivity with an increase in grain size. Carrier concentration measurements on these samples revealed that the higher conductivity of samples with small domains correlates with a higher carrier concentration, 8.6×10^{20} and 7.4×10^{19} cm^{-3} for samples A and B, respectively. These values are 1−2 orders of magnitude higher than the reported values for the CTS.[26] However, other Cu−Sn−S-based compounds with higher Cu/Sn ratios presented increasing carrier concentration with increasing Cu/Sn ratio, that is, 2.6×10^{21} and 5.6×10^{21} cm^{-3} for $Cu_7Sn_3S_{10}$[41] and $Cu_5Sn_2S_7$,[16] respectively. Sample A
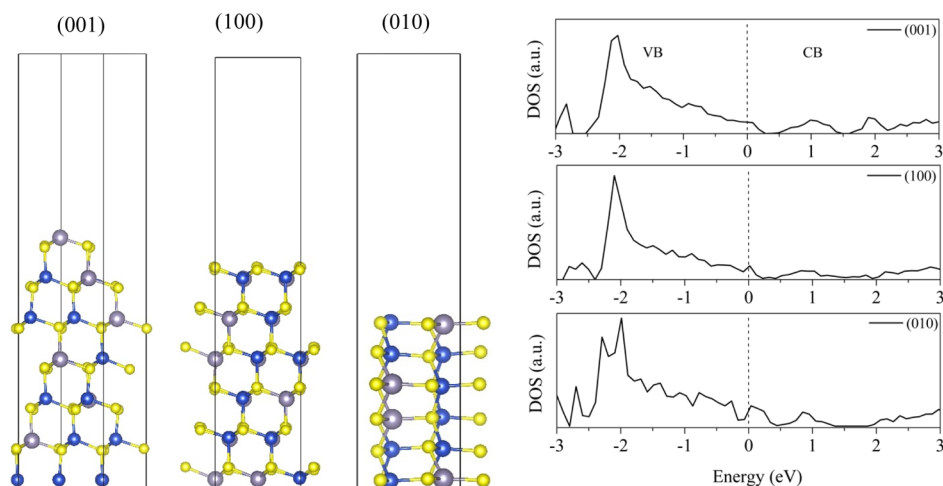
Figure 5. Monoclinic (ordered) CTS slabs with orientations (001), (100), and (010) and corresponding DOS plots. Here, the Fermi level is set to zero. Cu, Sn, and S atoms are represented by blue, gray, yellow colors, respectively.
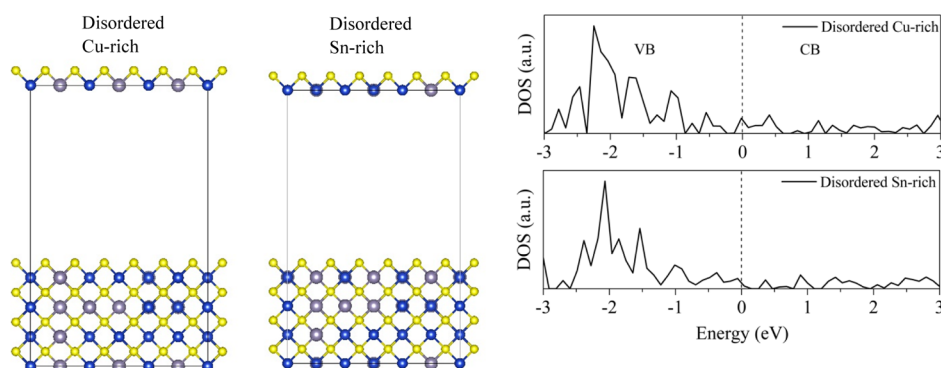
Figure 6. Structures and corresponding DOS for two disordered structures, where one has a Cu-rich and the other has a Sn-rich layer, just below the terminating sulfur layer. Here, the Fermi level is set to zero.

Table 2. Energy of the System, Formation Energy, and Formation Energy per Unit Atom for Various CTS Systems

system	configuration	energy of the system (eV)	formation energy (eV)	formation energy per unit atom (eV/atom)
CTS	24-Cu, 12-Sn, and 36-S	−308.0450	−23.8016	−0.3306
Cu-vacant	23-Cu, 12-Sn, and 36-S	−303.7652	−23.2520	−0.3275
Cu-rich	25-Cu, 11-Sn, and 36-S	−307.5523	−23.42630	−0.3254
Sn-rich	23-Cu, 13-Sn, and 36-S	−306.7465	−22.38570	−0.3109
Sn-vacant	24-Cu, 11-Sn, and 36-S	−302.2878	−21.8920	−0.3083

sintered at a low sintering temperature has a lower carrier mobility (1.2 cm^2/V s) than sample B (2.1 cm^2/V s), which is explained by the larger carrier concentration (increased probability of charge carrier collision) and lower grain size in sample A.

Due to the decreased electrical resistivity, sample A shows the highest *PF* value of ∼4.5 μW/K^2 cm, above 650 K, which is 3-fold and 9-fold higher than cubic (disordered) CTS (*PF* ∼1.5 μW/K^2 cm)[26] and monoclinic (ordered) CTS (*PF* ∼0.47 μW/K^2 cm),[14] respectively. Samples B and C have comparatively lower *PF* values of ∼1.5 and ∼1.2 μW/K^2 cm, respectively. The thermal diffusivity measurements are shown in Figure 4(iv). It is evident from the data that samples with smaller domains (more conductive) have a higher diffusivity. From the above considerations, it appears that the electrical properties are strongly dependent on the sintering temperature and grain size. Additional results following the same trend of the Seebeck coefficient and electrical resistivity with grain size support this statement (Figure S7). As mentioned above, a slight stoichiometric deviation can occur in the small grains due to the incomplete reaction and crystallization at low temperature, leading to high carrier concentration and electrical conductivity. The fast kinetics of the reaction and crystallization during SPS may also lead to variation of compositions at the grain surfaces and boundaries, which could be highly conductive and possibly injecting additional charge carriers in the system.

To investigate this further, three ordered and two disordered CTS surfaces (shown in Figures 5 and 6, respectively) were studied. The first three images in Figure 5 show ordered CTS slabs with (001), (010), and (100) planes. The other two images show disordered structures consisting of a Cu-rich layer and a Sn-rich layer, just below the terminating sulfur layer. Please note that the overall chemistry of the CTS system was respected while making all the structures shown in Figures 5 and 6. For each structure in Figures 5 and 6, the corresponding DOS are shown with the structures. After minimization, large distortions were observed for the surface atoms of all the structures. The reason is that surface atoms form incomplete bonds due to the change in the coordination number caused by the surface termination. The DOS on the VB side is higher than that on the CB side, showing p-type nature. However, no band gap was observed, suggesting a metallic character of all the studied structures. The localized states are visible near the Fermi level due to the dangling bonds on the surface. These dangling bonds provide additional charge carriers (holes), which increase the carrier concentration, leading to the degenerate semiconductor-like behavior observed in Figure 4. We are aware that the calculated structures are not an exact model of the grain boundary effects. Since the grains could terminate with any plane or orientation (favored by the local environment), these calculations only make the hypothesis plausible that CTS grains should have dangling bonds, which would lead to localized states at the Fermi level and increased electrical conductivity. These results are in agreement with a recent report by Dahule et al.,[29] although limited to the monoclinic phase.

Table 2 reports the formation energy per unit atom for vacancy and off-stoichiometry in CTS, as obtained from DFT simulations. It is evident from the reported values that after the stoichiometric CTS, Cu-vacant and Cu-rich systems are energetically more viable, whereas Sn-vacant and Sn-rich systems seem less likely to form. The corresponding DOS plots are shown in Figure S6. Thermodynamically, these conclusions could be generalized to the whole family of Cu−Sn−S systems. In other Cu−Sn−S systems, Cu-vacant and Cu-rich systems would be more likely to form than Sn-rich and Sn-poor phases. Moreover, in this family of materials, Cu vacancy, Cu excess, and Sn vacancy would enable p-type doping-like effects, whereas Sn excess showed n-type behavior.

The thermal conductivity and figure of merit are shown in Figure 7(i,ii), respectively. Since we are considering the heat capacity well above the Debye temperature (θ_D ∼213 K), the total thermal conductivity was calculated considering a constant value of Cp ∼0.44 J/g K for all samples. The total thermal conductivity for all samples decreases with temper-

F
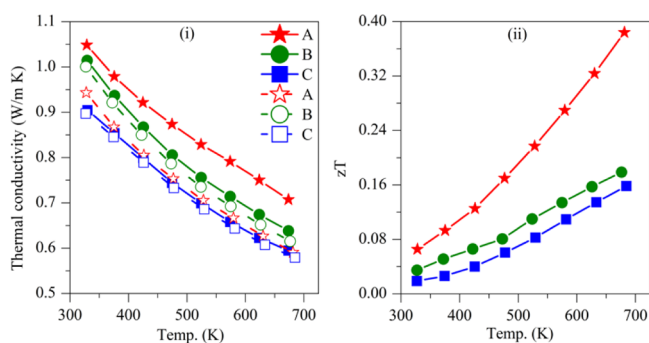
Figure 7. Temperature-dependent (i) total thermal conductivity (filled markers connected with the solid line) and lattice component of thermal conductivity (empty markers connected with the dashed line) and (ii) figure of merit.

ature due to an increased phonon−phonon interaction (Umklapp process or U-process). The electronic part of thermal conductivity (κ_e) was estimated according to the Wiedemann−Franz law (see equation 3), where the Lorenz number (L) was calculated using eq 4.[43]

$$L = 1.5 + e^{-\left(\frac{|S|}{116}\right)} \qquad (4)$$

where L is in 10^{-8} WΩ/K² and S in μV/K.

It is evident from Figure 7(i) that at higher temperatures, the lattice part of thermal conductivity is similar for all the samples, $\kappa_l \sim 0.6$ W/m K, above 673 K. This value is comparatively lower than the diamond-like CuFeS$_{2+x}$ system, where $\kappa_l \sim 1.0$ W/m K is reported at 650 K.[44] However, other Cu−Sn−S-based compounds such as Cu$_3$SnS$_4$ and Cu$_7$SnS$_{10}$ show a similar κ_l around 650 K, which further decreases to κ_l ~ 0.4 W/m K at 750 K.[40,41] The electronic contribution of thermal conductivity is the highest for sample A, and it decreases for samples B and C. This agrees with the corresponding resistivity and carrier concentration measurements as samples A, B, and C have increasing resistivity (decreasing carrier concentration) in the same order. The figures of merit of samples A, B, and C are equal to 0.40, 0.17, and 0.14 at 673 K, respectively. Overall, the two-step production method can be used to produce high-density nanostructured pellets. The experimental results indicate that a similar zT is reported for Cu$_{2+x}$Sn$_{1-x}$S$_3$ systems with Sn substitution ($x = 0.2$) by Zn,[14] Ni,[17] In,[25] and so forth.

CONCLUSIONS

We have studied the effects of crystalline domain size on the TE properties using experimental analyses and first-principles simulations. A CTS powder was produced from elemental powders (Cu, Sn, and S) by high-energy reactive ball milling, and subsequently, high-density pellets were produced using SPS. This method adds a distinct advantage by maintaining the nanostructure while reaching the required high density. Rietveld refinement of the XRD patterns revealed average domain sizes below 50 nm for samples sintered under different conditions. Low-temperature SPS sintering of mechanically alloyed powders allows to maintain structural disorder of the CTS phase while resulting in nanostructured ceramics. This leads to extremely low lattice thermal conductivity. On the other hand, the sample with the smallest average domain size also presents the lowest resistivity and Seebeck coefficient, resulting in the highest PF. Experimental evidence suggests that S and ρ correlate with the sintering temperature, which

induces stoichiometric deviations and different grain sizes. First-principles (DFT) simulations of three ordered and two disordered surfaces revealed the presence of dangling bonds and localized states near the Fermi level. DOS at the Fermi level was continuous, that is, band gap was absent, suggesting that CTS grain boundary is conductive. Formation energies for stoichiometric CTS, Cu-vacant, Cu-rich, Sn-vacant, and Sn-rich CTS are in the increasing order, implying that stoichiometric CTS is energetically the most favorable, followed by Cu-vacant and Cu-rich systems. The Cu-vacant, Cu-rich, and Sn-vacant systems increase the p-type behavior and carrier concentration, thus explaining the observed low resistivity of the sintered components. The samples with average domain sizes of 12 ± 10, 25 ± 10, and 37 ± 10 nm displayed figures of merit zT of 0.40, 0.17, and 0.14, respectively, around 673 K. The results presented here for various CTS surfaces, formation energies, and doping effects can be generalized to a broad family of Cu−Sn−S-based systems. Our synthesis method also provides an interesting route for many materials to synergistically tune their electrical and thermal properties.

ASSOCIATED CONTENT

Supporting Information

The Supporting Information is available free of charge at https://pubs.acs.org/doi/10.1021/acsaem.1c02377.

SEM−EDX data on 60-min milled CTS powder, Rietveld refinement data, corresponding EDX data for Figure 2, comparative SEM−EDX data for unpolished and polished samples A and B, temperature-dependent absolute Seebeck coefficient and resistivity for various CTS samples with increasing average domain size, and DOS for stoichiometric, Cu-vacant, Cu-rich, Sn-vacant, and Sn-rich CTS systems (PDF)

AUTHOR INFORMATION

Corresponding Authors

Emmanuel Guilmeau − *CRISMAT, CNRS, Normandie Univ, ENSICAEN, UNICAEN, 14000 Caen, France;* orcid.org/0000-0001-7439-088X; Email: emmanuel.guilmeau@ensicaen.fr

Paolo Scardi − *Department of Civil, Environmental & Mechanical Engineering, University of Trento, 38123 Trento, Italy;* orcid.org/0000-0003-1097-3917; Email: paolo.scardi@unitn.it

Authors

Ketan Lohani − *Department of Civil, Environmental & Mechanical Engineering, University of Trento, 38123 Trento, Italy;* orcid.org/0000-0003-1059-6744

Himanshu Nautiyal − *Department of Civil, Environmental & Mechanical Engineering, University of Trento, 38123 Trento, Italy;* orcid.org/0000-0003-2103-4130

Narges Ataollahi − *Department of Civil, Environmental & Mechanical Engineering, University of Trento, 38123 Trento, Italy;* orcid.org/0000-0002-8135-6054

Krishnendu Maji − *CRISMAT, CNRS, Normandie Univ, ENSICAEN, UNICAEN, 14000 Caen, France*

Complete contact information is available at:
https://pubs.acs.org/10.1021/acsaem.1c02377

Author Contributions

Notes

The authors declare no competing financial interest.

■ ACKNOWLEDGMENTS

■ REFERENCES

(1) Mao, J.; Liu, Z.; Zhou, J.; Zhu, H.; Zhang, Q.; Chen, G.; Ren, Z. Advances in Thermoelectrics. *Adv. Phys.* **2018**, *67*, 69−147.

(2) Jaldurgam, F. F.; Ahmad, Z.; Touati, F. Low-Toxic, Earth-Abundant Nanostructured Materials for Thermoelectric Applications. *Nanomaterials* **2021**, *11*, 895.

(3) Wei, T.-R.; Qin, Y.; Deng, T.; Song, Q.; Jiang, B.; Liu, R.; Qiu, P.; Shi, X.; Chen, L. Copper Chalcogenide Thermoelectric Materials. *Sci. China Mater.* **2019**, *62*, 8−24.

(4) Suekuni, K.; Kim, F. S.; Nishiate, H.; Ohta, M.; Tanaka, H. I.; Takabatake, T. High-Performance Thermoelectric Minerals: Colusites $Cu_{26}V_2M_6S_{32}$ (M = Ge, Sn). *Appl. Phys. Lett.* **2014**, *105*, 132107.

(5) Guélou, G.; Lemoine, P.; Raveau, B.; Guilmeau, E. Recent Developments in High-Performance Thermoelectric Sulphides: An Overview of the Promising Synthetic Colusites. *J. Mater. Chem. C* **2021**, *9*, 773−795.

(6) Biswas, K.; Zhao, L.-D.; Kanatzidis, M. G. Tellurium-Free Thermoelectric: The Anisotropic n-Type Semiconductor Bi_2S_3. *Adv. Energy Mater.* **2012**, *2*, 634−638.

(7) Tan, G.; Hao, S.; Zhao, J.; Wolverton, C.; Kanatzidis, M. G. High Thermoelectric Performance in Electron-Doped $AgBi_3S_5$ with Ultralow Thermal Conductivity. *J. Am. Chem. Soc.* **2017**, *139*, 6467−6473.

(8) Powell, A. V. Recent Developments in Earth-Abundant Copper-Sulfide Thermoelectric Materials. *J. Appl. Phys.* **2019**, *126*, 100901.

(9) Baláž, P.; Achimovičová, M.; Baláž, M.; Chen, K.; Dobrozhan, O.; Guilmeau, E.; Hejtmánek, J.; Knížek, K.; Kubíčková, L.; Levinský, P.; Puchý, V.; Reece, M. J.; Varga, P.; Zhang, R. Thermoelectric Cu−S-Based Materials Synthesized via a Scalable Mechanochemical Process. *ACS Sustainable Chem. Eng.* **2021**, *9*, 2003−2016.

(10) Snyder, G. J.; Toberer, E. S. Complex Thermoelectric Materials. *Nat. Mater.* **2008**, *7*, 105−114.

(11) Beretta, D.; Neophytou, N.; Hodges, J. M.; Kanatzidis, M. G.; Narducci, D.; Martin-Gonzalez, M.; Beekman, M.; Balke, B.; Cerretti, G.; Tremel, W.; Zevalkink, A.; Hofmann, A. I.; Müller, C.; Dörling, B.; Campoy-Quiles, M.; Caironi, M. Thermoelectrics: From History, a Window to the Future. *Mater. Sci. Eng., R* **2018**, *138*, 100501.

(12) Zhang, X.; Bu, Z.; Shi, X.; Chen, Z.; Lin, S.; Shan, B.; Wood, M.; Snyder, A. H.; Chen, L.; Snyder, G. J.; Pei, Y. Electronic Quality Factor for Thermoelectrics. *Sci. Adv.* **2020**, *6*, No. eabc0726.

(13) Dias, S.; Kumawat, K.; Biswas, S.; Krupanidhi, S. B. Solvothermal Synthesis of Cu_2SnS_3 Quantum Dots and Their Application in Near-Infrared Photodetectors. *Inorg. Chem.* **2017**, *56*, 2198−2203.

(14) Shen, Y.; Li, C.; Huang, R.; Tian, R.; Ye, Y.; Pan, L.; Koumoto, K.; Zhang, R.; Wan, C.; Wang, Y. Eco-Friendly p-Type Cu_2SnS_3 Thermoelectric Material: Crystal Structure and Transport Properties. *Sci. Rep.* **2016**, *6*, 32501.

(15) Lohani, K.; Isotta, E.; Ataollahi, N.; Fanciulli, C.; Chiappini, A.; Scardi, P. Ultra-Low Thermal Conductivity and Improved Thermoelectric Performance in Disordered Nanostructured Copper Tin Sulphide (Cu_2SnS_3, CTS). *J. Alloys Compd.* **2020**, *830*, 154604.

(16) Pavan Kumar, V.; Lemoine, P.; Carnevali, V.; Guélou, G.; Lebedev, O. I.; Boullay, P.; Raveau, B.; Al Rahal Al Orabi, R.; Fornari, M.; Prestipino, C.; Menut, D.; Candolfi, C.; Malaman, B.; Juraszek, J.;

Guilmeau, E. Ordered Sphalerite Derivative $Cu_5Sn_2S_7$: A Degenerate Semiconductor with High Carrier Mobility in the Cu−Sn−S Diagram. *J. Mater. Chem. A* **2021**, *9*, 10812−10826.

(17) Xu, X.; Zhao, H.; Hu, X.; Pan, L.; Chen, C.; Li, D.; Wang, Y. Synergistic Role of Ni-Doping in Electrical and Phonon Transport Properties of $Cu_2Sn_{1-X}Ni_XS_3$. *J. Alloys Compd.* **2017**, *728*, 701−708.

(18) Zhai, Y.-T.; Chen, S.; Yang, J.-H.; Xiang, H.-J.; Gong, X.-G.; Walsh, A.; Kang, J.; Wei, S.-H. Structural Diversity and Electronic Properties of Cu_2SnX_3 (X=S, Se): A First-Principles Investigation. *Phys. Rev. B: Condens. Matter Mater. Phys.* **2011**, *84*, 075213.

(19) Shigemi, A.; Maeda, T.; Wada, T. First-Principles Calculation of Cu_2SnS_3 and Related Compounds. *Phys. Status Solidi B* **2015**, *252*, 1230−1234.

(20) Zhao, H.; Xu, X.; Li, C.; Tian, R.; Zhang, R.; Huang, R.; Lyu, Y.; Li, D.; Hu, X.; Pan, L.; Wang, Y. Cobalt-Doping in Cu_2SnS_3: Enhanced Thermoelectric Performance by Synergy of Phase Transition and Band Structure Modification. *J. Mater. Chem. A* **2017**, *5*, 23267−23275.

(21) Deng, T.; Qiu, P.; Song, Q.; Chen, H.; Wei, T.-R.; Xi, L.; Shi, X.; Chen, L. Thermoelectric Properties of Non-Stoichiometric $Cu_{2+X}Sn_{1-X}S_3$ Compounds. *J. Appl. Phys.* **2019**, *126*, 085111.

(22) Zhao, L.; Chen, C.; Pan, L.; Hu, X.; Lu, C.; Wang, Y. Magnetic Iron Doping in Cu_2SnS_3 Ceramics for Enhanced Thermoelectric Transport Properties. *J. Appl. Phys.* **2019**, *125*, 095107.

(23) Zhang, Z.; Zhao, H.; Wang, Y.; Hu, X.; Lyu, Y.; Cheng, C.; Pan, L.; Lu, C. Role of Crystal Transformation on the Enhanced Thermoelectric Performance in Mn-Doped Cu_2SnS_3. *J. Alloys Compd.* **2019**, *780*, 618−625.

(24) Aihara, N.; Matsumoto, Y.; Tanaka, K. Exciton Luminescence from Cu_2SnS_3 Bulk Crystals. *Appl. Phys. Lett.* **2016**, *108*, 092107.

(25) Tan, Q.; Sun, W.; Li, Z.; Li, J.-F. Enhanced Thermoelectric Properties of Earth-Abundant Cu_2SnS_3 via In Doping Effect. *J. Alloys Compd.* **2016**, *672*, 558−563.

(26) Lohani, K.; Nautiyal, H.; Ataollahi, N.; Fanciulli, C.; Sergueev, I.; Etter, M.; Scardi, P. Experimental and Ab Initio Study of Cu_2SnS_3 (CTS) Polymorphs for Thermoelectric Applications. *J. Phys. Chem. C* **2021**, *125*, 178−188.

(27) Siyar, M.; Cho, J.-Y.; Youn, Y.; Han, S.; Kim, M.; Bae, S.-H.; Park, C. Effect of Annealing Temperature on the Phase Transition, Band Gap and Thermoelectric Properties of Cu_2SnSe_3. *J. Mater. Chem. C* **2018**, *6*, 1780−1788.

(28) Baranowski, L. L.; McLaughlin, K.; Zawadzki, P.; Lany, S.; Norman, A.; Hempel, H.; Eichberger, R.; Unold, T.; Toberer, E. S.; Zakutayev, A. Effects of Disorder on Carrier Transport in Cu_2SnS_3. *Phys. Rev. Appl.* **2015**, *4*, 044017.

(29) Dahule, R.; Raghav, A.; Hanindriyo, A. T.; Hongo, K.; Maezono, R.; Panda, E. Surface Study of Cu_2SnS_3 Using First-Principles Density Functional Theory. *Adv. Theory Simul.* **2021**, *4*, 2000315.

(30) Baláž, P.; Dutková, E.; Levinský, P.; Daneu, N.; Kubíčková, L.; Knížek, K.; Baláž, M.; Navrátil, J.; Kašparová, J.; Ksenofontov, V.; Möller, A.; Hejtmánek, J. Enhanced Thermoelectric Performance of Chalcopyrite Nanocomposite via Co-Milling of Synthetic and Natural Minerals. *Mater. Lett.* **2020**, *275*, 128107.

(31) Kresse, G.; Furthmüller, J. Efficient Iterative Schemes for Ab Initio Total-Energy Calculations Using a Plane-Wave Basis Set. *Phys. Rev. B: Condens. Matter Mater. Phys.* **1996**, *54*, 11169−11186.

(32) Kresse, G.; Furthmüller, J. Efficiency of Ab-Initio Total Energy Calculations for Metals and Semiconductors Using a Plane-Wave Basis Set. *Comput. Mater. Sci.* **1996**, *6*, 15−50.

(33) Perdew, J. P.; Burke, K.; Ernzerhof, M. Generalized Gradient Approximation Made Simple. *Phys. Rev. Lett.* **1996**, *77*, 3865−3868.

(34) Pack, J. D.; Monkhorst, H. J. "Special Points for Brillouin-Zone Integrations"-a Reply. *Phys. Rev. B: Solid State* **1977**, *16*, 1748−1749.

(35) Scardi, P.; Leoni, M. Diffraction Line Profiles from Polydisperse Crystalline Systems. *Acta Crystallogr., Sect. A: Found. Crystallogr.* **2001**, *57*, 604−613.

(36) Coelho, A. A. TOPAS and TOPAS-Academic: An Optimization Program Integrating Computer Algebra and Crystallographic Objects Written in C++. *J. Appl. Crystallogr.* **2018**, *51*, 210−218.

(37) Scardi, P.; Azanza Ricardo, C. L.; Perez-Demydenko, C.; Coelho, A. A. Whole Powder Pattern Modelling Macros for TOPAS. *J. Appl. Crystallogr.* **2018**, *51*, 1752−1765.

(38) Black, D. R.; Mendenhall, M. H.; Brown, C. M.; Henins, A.; Filliben, J.; Cline, J. P. Certification of Standard Reference Material 660c for Powder Diffraction. *Powder Diffr.* **2020**, *35*, 17−22.

(39) McCusker, L. B.; Von Dreele, R. B.; Cox, D. E.; Louër, D.; Scardi, P. Rietveld Refinement Guidelines. *J. Appl. Crystallogr.* **1999**, *32*, 36−50.

(40) Yang, Y.; Ying, P.; Wang, J.; Liu, X.; Du, Z.; Chao, Y.; Cui, J. Enhancing the Thermoelectric Performance of Cu_3SnS_4 -Based Solid Solutions through Coordination of the Seebeck Coefficient and Carrier Concentration. *J. Mater. Chem. A* **2017**, *5*, 18808−18815.

(41) Deng, T.; Qiu, P.; Xing, T.; Zhou, Z.; Wei, T.-R.; Ren, D.; Xiao, J.; Shi, X.; Chen, L. A Low-Cost and Eco-Friendly Br-Doped $Cu_7Sn_3S_{10}$ thermoelectric Compound With zT around Unity. *J. Mater. Chem. A* **2021**, *9*, 7946−7954.

(42) Narducci, D.; Selezneva, E.; Cerofolini, G.; Frabboni, S.; Ottaviani, G. Impact of Energy Filtering and Carrier Localization on the Thermoelectric Properties of Granular Semiconductors. *J. Solid State Chem.* **2012**, *193*, 19−25.

(43) Kim, H.-S.; Gibbs, Z. M.; Tang, Y.; Wang, H.; Snyder, G. J. Characterization of Lorenz Number with Seebeck Coefficient Measurement. *APL Mater.* **2015**, *3*, 041506.

(44) Xie, H.; Su, X.; Yan, Y.; Liu, W.; Chen, L.; Fu, J.; Yang, J.; Uher, C.; Tang, X. Thermoelectric Performance of $CuFeS_{2+2x}$ Composites Prepared by Rapid Thermal Explosion. *NPG Asia Mater.* **2017**, *9*, No. e390.